Commissioning of the NACO Fabry-Perot Interferometer at the VLT

Markus Hartung[a], Chris Lidman[a], Nancy Ageorges[a], Olivier Marco[a], Markus Kasper[b], and Yann Clenet[b]

[a]European Southern Observatory, Casilla 19, Santiago, Chile;
[b]European Southern Observatory, Karl-Schwarzschild-Str. 2, 85748 Garching, Germany

ABSTRACT

In October 2002 the VLT Adaptive Optics (AO) facility instrument NAOS-CONICA (NACO) was offered for the first time to the astronomical community and has been operated successfully ever since. NACO is capable of performing AO assisted imaging, spectroscopy, polarimetry, and coronography. One exciting and unique observing capability of NACO is its cold tunable Fabry-Perot Interferometer, that will be offered in October 2004. The 3-dimensional structure analysis of extended objects, such as planetary nebulae, is one interesting application of this device that combines imaging and medium resolution spectroscopy in the K-band. Using VLT day and night time commissioning data, the performance of the Fabry-Perot is evaluated and a strategy to handle the complex calibration and data reduction has been developed.

Keywords: Fabry-Perot Interferometer, Adaptive Optics, NACO, VLT

1. INTRODUCTION

In this article we describe the main results from the commissioning of the cryogenic Queensgate Fabry-Perot (FP) mounted in the collimated beam of the near-infrared camera CONICA[1] which is fed by the NAOS AO system.[2,3] This FP is tunable from 2.0 to 2.5 μm, whereby a set of 18 intermediate band order-sorting filters (FWHM 60 nm) block the light of unwanted orders. In combination with AO at an 8-m-class telescope, the NACO FP is a unique facility device. Observing and calibration templates are under development to ensure the scientific output in terms of completeness and reliability of on-sky and calibration data. We investigate the achievable performance in stability and tuning accuracy and the implied aspects for the observing strategy. Even if we focus on the NACO FP, this article may be helpful for other FP setups, or in general to those who want to use a FP for astronomical observations.

FP observations are known to be complex and expensive in observing time. The data reduction, in particular the accurate phase map correction, does not appear straight forward and many observers are inclined to avoid a FP at all. It is intended to facilitate the use of this device and to mitigate the reluctance towards FP applications. Even if the phase map correction is treated in more detail in this article, in many cases it is not needed, and the NACO FP can simply be used as a *tunable filter*. Astrophysical FP applications span a wide range, e.g., distant emission line objects, internal dynamics of emission line nebulae and relatively nearby galaxies, or even QSO and radio galaxy environments studies; atmospheric variability of brown dwarfs; detection and mapping of selected chemical compounds for solar system objects; etc.[4] - without doubt, FP imaging significantly expands the capability of VLT instrumentation and opens exciting possibilities in 3D structure analysis (velocity mapping).

For the reader's convenience we first compile the principal formulas (Sect. 2), then we explain the calibration of the relation between wavelength, order, and the plate distance with a particular eye mark on small corrections that are needed for accurate line matching over the whole tuning range (Sect. 3). After investigating the FP cavity stability (Sect. 4), we focus on the phase map correction (Sec. 5) and demonstrate the procedure on the example of an Argon calibration line and the Brγ emission line of the planetary nebula IC 418 ("spirograph" nebula).

Send offprint requests to: M. Hartung, e-mail: mhartung@eso.org

2. SHORT REVIEW OF PRINCIPLES

The theory of Fabry-Perot interferometers is based on multiple reflections at planar surfaces.[5] The transmission is described by the Airy formula:

$$\frac{I_\mathrm{t}}{I_\mathrm{i}} = \frac{1}{1 + F \sin^2 \frac{\delta}{2}} \ , \tag{1}$$

where I_i and I_t denote the intensity of the incoming and the transmitted beam respectively. The quality of the spectral separation is described by

$$F = \frac{4R}{(1-R)^2} \ , \tag{2}$$

with R being the reflectivity of a simple plate. The phase shift δ is given by

$$\delta = \frac{4\pi}{\lambda} n d \cos\theta \ , \tag{3}$$

where λ represents the wavelength, n the refractive index, d the plate thickness (or separation), and θ the inclination angle. The finesse

$$f = \frac{\pi\sqrt{F}}{2} \tag{4}$$

measures the ratio of the separation of two peaks coming from adjacent orders and their FWHM.

3. CALIBRATION OF WAVELENGTH, ORDER, AND PLATE DISTANCE

The astronomer who selects the observing wavelength λ needs to know at what order m the FP provides the best performance, and what plate separation d he needs for an optimal scan of the field of view (FOV). The FOV has to be scanned because of the inclination dependent interference condition, i.e., only a ring-shaped part of the FOV is transmitted for a selected wavelength (see Sect. 5). This is typical for a collimated FP setup. Hence, care must be taken regarding the sampling of the wavelength channel as well as the completeness of the data cube. A spatial calibration of the phase-shift dependence for the whole FOV is undertaken via a *phase map*. The construction of the phase map and its application on a set of calibration and on-sky data is explained later on.

To calibrate the wavelength dependency of the plate separation d, controlled by the "z-value" given in Fabry-Perot Control Units (FCU), continuum light is directed into the 86-mas Slit and dispersed with Grism 3.* Undesired orders from the grism are suppressed by the K-band filter, and we use Camera S27 (27 mas/pix) for appropriate sampling. Deploying the FP will cut out the images of the slit according to the interference condition for a parallel beam:

$$m\lambda = 2d. \tag{5}$$

In this configuration, a stack of frames for different z-values is taken (calibration data cube). Figure 1 shows the frame for $z = -100$ FCU, i.e. almost at the middle of the FP's tuning range. Using the 27 mas pixel scale, typically six to eight different orders can be seen. The slight bending of the dispersed slit images is due to the phase shift, according to the interference condition dependent on the inclination angle (Eq. 3, Eq. 10). *The higher the inclination angle, the shorter the wavelength transmitted by the FP.* This is the reason why the horizontal lines in Fig. 1 are bent towards lower wavelengthss (downwards) at both sides of the FOV.

Now, we focus on the calibration of the $\lambda(z)$-relation for the perpendicular case (zero inclination angle). For accurate tuning of the FP, sub-nanometer accuracy in wavelength is needed; hence, a K-band calibration spectrum of Argon lines should be taken just before. The dispersion of the grism must be modeled in second order.

The wavelength belonging to the different orders is extracted. This is done for each frame of the data cube. The data cube contains the scan positions ranging from $z = -500$ FCU to $z = +500$ FCU in steps of 100 FCU. The wavelength information is extracted in the center of the FOV to avoid any inclination of the beam passing

*Spectroscopic mode S27_Grism3: dispersion 2.0 pix/nm, spectral resolution 1500. A detailed instrument description can be found under `http://www.eso.org/instruments/naos/`.

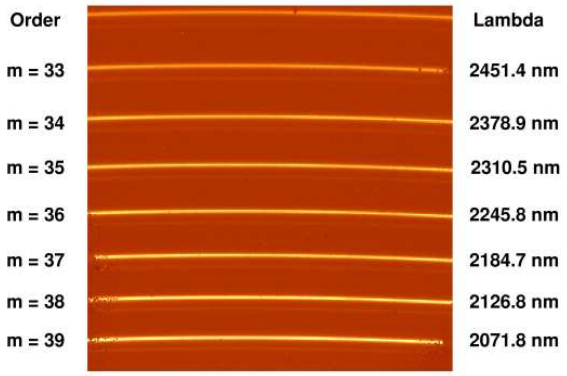

Figure 1. A sample frame at $z = -100$ FCU from the calibration cube to determine the relation between the wavelength λ and the plate separation z. The spectroscopic mode S27_Grism3 (Slit 86 mas, K-filter) is used in combination with the FP. Illumination with *continuum light*. The direction of dispersion is vertical. The image of the entrance slit is seen in eight successive orders ranging from $m = 32$ (top) to 40 (bottom). Increasing the plate separation during the scan shifts the lines further upwards and higher orders will appear from the bottom. Compare with Table 1.

the FP. Table 1 contains the wavelength and z information extracted from the calibration data cube. To assign the correct order to the extracted wavelength, we calculate a number of regression lines for different hypothetical values of m_0, whereby the n extracted wavelengths are denoted by λ_0 through λ_n. Then we can find the m_0 that fulfills

$$\lambda_n \cdot m_0 = \lambda_{n-1} \cdot (m_0 + 1) = \lambda_{n-2} \cdot (m_0 + 2) = ... = \lambda_0 \cdot (m_0 + n) \tag{6}$$

with the least square deviation. This 'order fitting' is repeated for each of the scan frames. From frame to frame, the orders shift successively upwards (Fig 1). Now we can determine for each order a linear relationship between z and λ using a regression line. These regression lines are plotted in Fig. 2.

Even if the available tuning range is twice as large, we confine ourselves to a scan region ranging from $z = -500$ to $z = +500$ FCU since this is the region where the piezo stack control behaves linearly and preserves plate parallelism. This restriction has no impact, because any line in the accessible wavelength band (K) can be scanned in multiple orders. Limiting the region of the tuning range from $z = -500$ to $z = +500$ FCU will only cancel the smallest and highest orders, which are not needed.

The described procedure to allocate the orders and determining the parameters of the regression lines ($\lambda(z)$-relation) only needs to be repeated after an intervention at the instrument, otherwise these parameters are very stable. The only measurement to be repeated before and after each FP observation is a quick scan (approximately 1-2 minutes) of an Argon calibration line to compensate for offsets (expressed through constant C, Eq. 9) that might be caused by drifts of the piezo stack.

Phase jump correction

The plate separation derived from different orders at zero inclination angle is expected to yield the constant value $2d$ (Eq. 5). Yet, if we calculate the plate separation using all wavelengths for the different orders, the values appear to drop monotonously with wavelength (Table 2). This is demonstrated at the example of the frame for $z = -100$ FCU shown in Fig. 3. The average plate separation $2d$ is subtracted from all values to point out the residual deviation from the expected constant. This residual deviation is of the order of 100 nm for all accessible wavelengths, i.e., a deviation of approximately $\pm 2.5\%$ from the K-band central wavelength. This effect may be explained by a wavelength dependent phase jump in the complex coating of the FP plate surfaces that we denote with $2\delta(\lambda)$[†]:

$$m \cdot \lambda + 2\delta(\lambda) = 2d = \underbrace{ma}_{A} + \underbrace{mb}_{B} \cdot z \ . \tag{7}$$

[†]The factor 2 reflects that the phase jump occurs at both surfaces of the FP cavity.

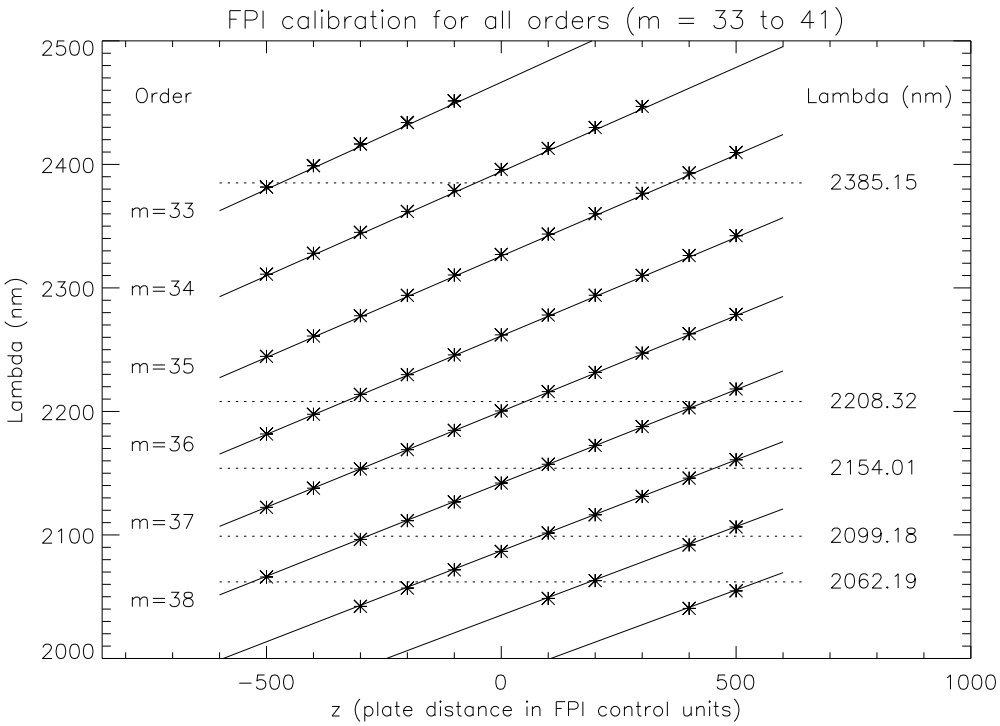

Figure 2. The plot shows the wavelengths extracted from 11 calibration frames ranging from $z = -500\,\mathrm{FCU}$ to $z = +500\,\mathrm{FCU}$ in steps of 100 FCU (compare Table 1). Regression lines for the different orders are shown. In addition, all available Argon calibration lines are indicated. This plot is important to prepare FP observations, i.e., to determine the appropriate order and to chose a calibration line at similar plate distance (z-value).

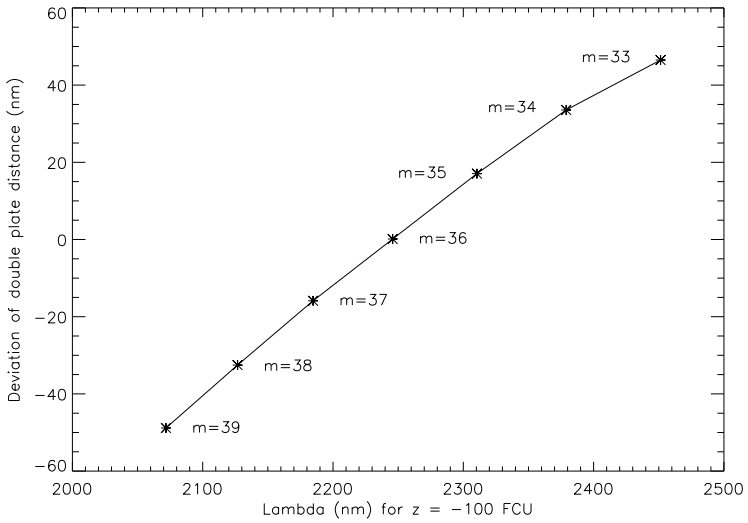

Figure 3. The plate separation determined via the regression line parameters for different orders plotted versus wavelength. The deviation from a horizontal straight line is explained by a wavelength-dependent phase jump occurring in the FP coating during the multiple reflections within the interference spacing.

Table 1. Extracted wavelengths for all z-positions of the calibration cube.

m	z (FCU)										
	-500	-400	-300	-200	-100	0	100	200	300	400	500
33	2381.64	2398.99	2416.52	2433.90	2451.38	-	-	-	-	-	-
34	2311.09	2328.00	2344.96	2361.93	2378.90	2395.93	2412.95	2429.88	2446.92	-	-
35	2244.56	2261.03	2277.49	2293.95	2310.46	2327.05	2343.59	2360.08	2376.61	2393.07	2409.60
36	2181.76	2197.73	2213.77	2229.78	2245.81	2261.99	2278.05	2294.07	2310.16	2326.20	2342.28
37	2122.34	2137.88	2153.47	2169.05	2184.68	2200.40	2216.04	2231.65	2247.29	2262.89	2278.54
38	2066.02	-	2096.36	2111.58	2126.75	2142.03	2157.27	2172.49	2187.76	2202.90	2218.18
39	-	-	2042.18	2056.97	2071.80	2086.70	2101.56	2116.34	2131.22	2146.01	2160.88
40	-	-	-	-	-	-	2048.63	2063.06	-	2091.94	2106.46
41	-	-	-	-	-	-	-	-	-	2040.55	2054.73

Table 2. Plate distance ($2d = m\lambda$) in nm determined for all z-positions of the calibration cube using the extracted wavelength of all available orders. Apparently, the values for $2d$ are not constant for fixed z. This effect is explained by a wavelength dependent phase jump occurring within the complex coating of the cavity surfaces. Neglecting the phase jump causes errors up to 30 Å in wavelength tuning.

z	m									σ	[max-min]
(FCU)	33	34	35	36	37	38	39	40	41	(nm)	(nm)
-500	78594.1	78577.1	78559.6	78543.4	78526.6	78508.8	-	-	-	31.7	85.3
-400	79166.7	79152.0	79136.1	79118.3	79101.6	-	-	-	-	25.9	65.1
-300	79745.2	79728.6	79712.1	79695.7	79678.4	79661.7	79645.0	-	-	36.1	100.
-200	80318.7	80305.6	80288.2	80272.1	80254.9	80240.0	80221.8	-	-	35.1	96.8
-100	80895.5	80882.6	80866.1	80849.2	80833.2	80816.5	80800.2	-	-	34.8	95.3
0	-	81461.6	81446.8	81431.6	81414.8	81397.1	81381.3	-	-	30.3	80.3
100	-	82040.3	82025.7	82009.8	81993.5	81976.3	81960.8	81945.2	-	34.6	95.1
200	-	82615.9	82602.8	82586.5	82571.0	82554.6	82537.3	82522.4	-	34.2	93.5
300	-	83195.3	83181.4	83165.8	83149.7	83134.9	83117.6	-	-	29.0	77.7
400	-	-	83757.5	83743.2	83726.9	83710.2	83694.4	83677.6	83662.6	34.6	94.8
500	-	-	84336.0	84322.1	84306.0	84290.8	84274.3	84258.4	84243.9	33.5	92.0

Table 3. Phase jump corrected plate distances ($2d = m\lambda + 2\delta(\lambda)$) in nm determined for all z-positions of the calibration cube using the extracted wavelength of all available orders. After correction for the phase jump $2\delta(\lambda)$ the values $2d$ stay constant with a relative error of $7 \cdot 10^{-4}$ %. With this correction term the wavelength tuning is accurate to 0.6 Å for all spacings and λ, m-combinations. A precision of 0.6 Å corresponds to 3 % of the FP bandpass (FWHM 2 nm). The remaining influence of this error to FP tuning is completely negligible.

z	m									σ	[max-min]
(FCU)	33	34	35	36	37	38	39	40	41	(nm)	(nm)
-500	78594.1	78577.1	78559.6	78543.4	78526.6	78508.8	-	-	-	0.7	2.0
-400	79104.5	79105.5	79105.8	79104.8	79105.1	-	-	-	-	0.5	1.3
-300	79679.4	79678.2	79677.8	79677.9	79677.4	79677.7	79678.2	-	-	0.6	2.0
-200	80249.4	80251.4	80249.8	80250.0	80249.4	80251.4	80250.2	-	-	0.9	2.1
-100	80822.8	80824.7	80823.7	80822.8	80823.3	80823.3	80823.9	-	-	0.6	1.8
0	-	81400.1	81400.4	81401.2	81400.6	81399.5	81400.3	-	-	0.6	1.7
100	-	81975.2	81975.5	81975.3	81975.0	81974.2	81975.3	81976.3	-	0.6	1.8
200	-	82547.4	82549.0	82548.1	82548.4	82548.2	82547.2	82548.9	-	0.7	1.8
300	-	83123.4	83123.9	83123.4	83123.0	83124.1	83123.1	-	-	0.4	1.1
400	-	-	83696.5	83697.1	83696.2	83695.3	83695.6	83695.0	83696.3	0.7	2.1
500	-	-	84271.6	84272.3	84271.4	84271.8	84271.2	84271.4	84273.1	0.7	1.9

Table 4. Summary of the FP calibration coefficients. The constant C is subject to fine adjustment before each FP observation to compensate for potential drifts. The Δz-value for a step of 1 nm varies from 6 to 7 FCU in dependence of order and wavelength.

	$z(\lambda)$ (FCU)			$2\delta(\lambda)$ (nm)	
A (nm)	B (nm/FCU)	C (FCU)	α	β (nm^{-1})	λ_0 (nm)
81400.6	5.74	-26.1	2.9037e-1	-1.6293e-4	2150.

The function $\delta(\lambda)$ describes the effective total phase shift per plate, which may involve multiple reflections. To enhance the precision of the z-calibration, we shall model this effect and take it into account. Using a second-order polynomial, a suitable model is

$$2\delta(\lambda) = \alpha \cdot (\lambda - \lambda_0) + \beta \cdot (\lambda - \lambda_0)^2 \ , \tag{8}$$

with its parameters summarized in Tab. 4. To express the calibration results (shown in Fig. 2 and described in Eq. 7) independent of the order, we use the parameters $A = ma$ and $B = mb$. Their values are given in Table 4. The coefficient A corresponds to the plate separation at $z = 0$, the middle position of the cavity's tuning range. Applying the small $\delta(\lambda)$-correction, the plate separation for a given z yields identical values, no matter what order-wavelength couple was used to calculate it (Table 3). The apparent contradiction is solved by the phase jump correction.

To set up the FP, we solve Eq. 7 for z and add a constant C, to adjust for small offsets that might be caused by drifts:

$$z = \frac{1}{B}(m\lambda + 2\delta(\lambda) - A) + C \ . \tag{9}$$

The constant C should be determined before and after each FP observation to directly detect and correct for a potential drift. Using a fast camera (S54), this is done with negligible loss of observing time (1-2 minutes) by scanning through an Argon calibration line at similar plate distances as used for the real observations. Having determined the calibration parameters including the correction for the wavelength dependent phase jump, we can set every wavelength over the whole tuning range within an accuracy better than 1 Å. Without the described phase jump correction, the calculated and the actual values can differ by several nm which is unacceptable for scientific applications. Since FP observations are time expensive and the S/N might be low, it is of highest importance that we are able to set the wavelength with high reliability.

4. DRIFT AND EXPOSURE STABILITY

FP scans can last several hours. If a potential drift of the FP exceeds a certain value during the observation or the scan (> 5 Å) the scientific exploitability is not warranted anymore. Inaccurate line matching will directly translate in a loss of S/N (or even worse, in an invalid data set, if completely off the line), and the wavelength error will degrade accordingly the precision of derived velocities.

The stability of the FP piezo stack was measured at three plate distances over a time interval of 72 minutes. Keeping the plate distance constant, a frame was taken every 8 minutes. The used plate distances were distributed over the whole tuning range, approximately in the middle and at the upper and lower limits (z=-510 FCU, +210 FCU, + 565 FCU). The z-values are not completely symmetric and centered since we need to match one of the available Argon calibration lines. We chose λ=2062.19 nm at $m = 38$, 40 and 41, see Fig. 2. The drift information was extracted by determining the peak of the ring at four cut positions: two horizontal opposing cut positions and two vertical opposing cut positions (Fig. 4, top left). To allow for a precise determination of the maximum, the frames were first smoothed (box car average with a width of 15 pixel) to suppress the wiggles, and then a gauss function was fitted to the values above a certain threshold value. The threshold value is selected rather high to avoid any influence of deviations from the gauss function.

The results are shown in Fig. 4. For the positions z=-510 FCU and +210 FCU, the FP behaved very stable, the deviations are less than 1 Å. In contrary, during the measurement at z=+565 a sudden drift of about

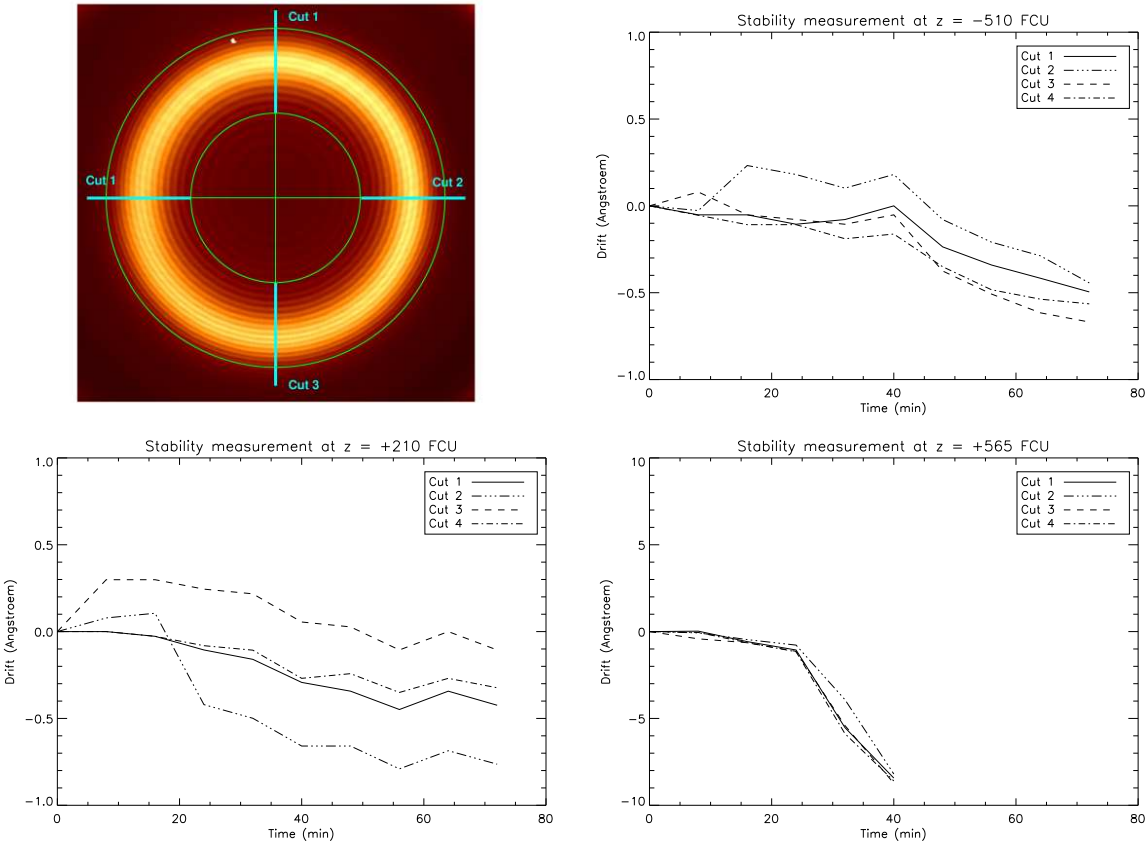

Figure 4. Stability of the plate distance during a long exposure: At three different spacings the time evolution of the monochromatic ring was tracked. The four curves shown in each plot correspond to the deviation of the ring over time. These deviations were measured at four cut positions that are arranged like a cross (top left). During the traced drift the cavity spacing remained parallel since the four curves stay close together. Drifts below 1 Å are completely negligible, but a sudden drift occurred for the measurement at $z = +565\,\mathrm{FCU}$ (bottom right).

10 Å occurred. Hence, it is mandatory to perform a quick test scan of a calibration line before and after the observations. Preferably, this scan should be done at plate distances similar to those used for the observation. The appropriate calibration line and order combination can be chosen from Fig. 2.

5. PHASE MAP CORRECTION

As already mentioned in Sect. 3, the interference condition varies radially over the field. Accordingly, the phase is shifted over the FOV.[6,7] The equation

$$m \cdot \lambda + 2\delta(\lambda) = \frac{2d}{\sqrt{1 + (\frac{r}{f})^2}} \tag{10}$$

describes how the interference condition changes for different inclination angles. The effective phase shift per plate $\delta(\lambda)$ is not to be neglected, since it may cause significant deviations over the full wavelength range, in particular when using a large FOV. The radial variation of the interference condition makes the calibration line appear as a monochromatic ring that is described by radius r and focal length f in consistent units. In a typical FP observation (scan), a stack of images taken at different plate separations constitute a data cube. Three scan positions of the 2154.01 nm Argon calibration line are displayed in the left image sequence of Fig. 6. According to the inclination dependent interference condition, the transmission ring spreads out over the FOV

for different plate separations, i.e, the FOV is scanned by the moving ring-shaped monochromatic area while the plate separation is modified. The shown intensity profiles indicate the spatial position in the FOV dependent on z (plate separation) where the corresponding z-frame transmits the calibration line. The rings show a substructure, i.e. intensity wiggles at a smaller scale than the FWHM of the ring. This small-scale intensity variation is due to interference emerging from the plates of the FP itself, and *not* from the tunable cavity. These small intensity variations (maximum 5% of total intensity) that are independent of the actual spacing, could be avoided using wedge-shaped plates. Nevertheless, this artifact does not affect data reduction. In general, astronomical data are not afflicted by this effect, since the intensity variations are small and the wiggles smear out for lines broader than 1 Å.

The actual wavelength information is restored by performing a phase correction that eventually allows one to retrieve the complete wavelength information over the FOV and to construct velocity maps. We now focus on the construction of the phase shift map for the calibration data.

Equation 10 is graphically presented in Fig. 5 using the parameters determined before (Table 4). A vertical cut through the phase maps for all cameras is shown. In Fig. 5 the necessary phase shift correction in wavelength is plotted over the position within the FOV: to the left in pixels and to the right in arcsec. The right curve describes the phase shift independent of the pixel scale. The FOVs of the four available camera objectives are indicated by the horizontal dotted lines. The CONICA pixel scales differ from each other by a factor of 2. Note, that Camera 100S is pupil limited. Using Eq. 10 and Eq. 9, the z-value is determined for a certain position of the FOV (x, y) and the selected wavelength. Since the data cube is taken at discrete z-values, intermediate positions of the (x, y, z)-cube have to be linearly interpolated. This interpolation must be done for all (x, y)-coordinates (all pixels of the frame) to cover the whole FOV. In this way, a frame at the spectral center of the calibration wavelength ($\lambda_{\rm cal} = 2154.01\,$nm) is generated (Fig. 6, right sequence). As expected, this frame is homogeneously illuminated (disregarding the wiggles). The black outer part of the frame is the region of the FOV where the transformation of the (x, y, z)- to a (x, y, λ)-frame has no data.

An important remark is that the phase map correction can be completely avoided in case that only a restricted FOV is needed. Since the FWHM of the FP is 2 nm, a wavelength shift up to 2 Å is completely negligible. According to Eq. 10 this corresponds to a circular region centered to the zero phase shift point (ZPP) of the FOV with a radius of approximately $4''$. The ZPP is not exactly identical with the center of the chip due to a small deviation from an ideally symmetric alignment.

Fabry-Perot scan of the planetary nebula IC 418

During nighttime commissioning IC 418 was observed as extended test object. The angular diameter approximately amounts to $14''$. This is significantly larger than $8''$, hence, phase map correction is mandatory, in particular if the object is not centered with respect to ZPP. The scan was repeated at three different positions of the FOV (center, upper right, lower left) to verify the procedure of phase map correction. Remind that the applied wavelength correction depends of the position of the FOV. Hence, moving the extended test object over the FOV means that completely different phase shifts have to be applied, but the resulting phase map corrected images must be the same. Exemplarily, we focus on the case were the nebula is positioned at the upper right, because here the effect of phase map correction is more dramatic. In this case the spectral variation over the planetary nebula amounts to approximately 6 nm. This compares to a spectral variation of 1 nm if the nebula would be centered with respect to the ZPP. At this point we note that if the observer wishes to use a jitter pattern and add up the data before or without correcting the phase shift, the jitter pattern should be small (ideally $< 1''$) to keep the phase shift negligible. Furthermore, the whole data cube should be taken first before moving to the next jitter position.

The strong Brγ-emission line (2166.7 nm) is scanned over a spectral region of 5.4 nm. Ten frames were taken with a constant step width of Δz=4 FCU corresponding to λ=0.6 nm. Hence, the spectral channel is oversampled by a factor of 1.7[‡] given a spectral response of 2 nm FWHM of the FP. The exposure time of each frame was 3x120 seconds, this yields to total exposure time of 3600 seconds for the cube at one offset position. Note that the exposure time could have been optimized by strict Nyquist sampling of the spectral channel, and constraining

[‡]If the Nyquist criterion corresponds to a oversampling factor of 1.

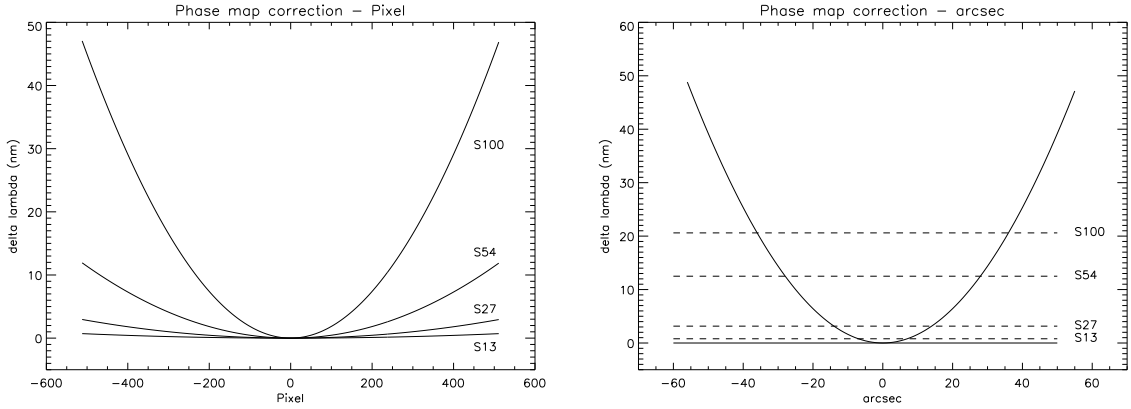

Figure 5. Phase maps for all cameras (vertical cuts): z-correction versus pixel coordinate and versus angle (arcsec). The representation in arcsec is independent of the camera objective. The corresponding FOV for the different objectives is indicated by dashed lines. The smaller the required FOV, the smaller the needed phase map correction.

the exposed space of the data cube to only the parts that are of scientific interest. For test reasons this was not done during commissioning.

The data cube is sky-corrected with one of the cubes at the other offset positions. The cube was flatfielded with an internal lamp flat (continuum light) taken with the FP deployed, the same order-sorting filter and a suitable spacing (mean value of the spacings applied for the on-sky scan). For the phase map correction we follow the procedure described above for the calibration line and generate a phase shift corrected frame centered on the Brγ-line (Fig. 6, left sequence). Independent of the offset position we achieve identical phase shift corrected frames (not shown), as expected for a correct application of the phase map. In principal, we can superpose the phase shift corrected frames, but one might risk a degradation of spatial resolution if the AO correction did not stay stable during the scans for different offset positions.

The sequence from $z = 146$ to 162 FCU is a striking demonstration of how the intensity flashes up for regions in the FOV where the monochromatic ring overlays the planetary nebula. Away from this region the line emission is blocked and only the continuum remains. Apparently, this continuum emission is much weaker. The phase shift corrected frame at 2166.1 nm shows the whole planetary nebula in Brγ-line emission. Creating phase shift corrected frames for the whole scanned spectral region with a step width of 0.5 nm (i.e, performing the complete transformation of the x, y, z-cube to the x, y, λ-cube) allows us to extract spectra for each pixel. The generation of a velocity map is straight-forward, in determining the spectral shift of the maximum of the emission line for each pixel. This application is in particular exciting regarding a spatial resolution of 50 mas, although IC 418 is less suitable for a demonstration of velocity mapping since the shell expands with approximately 15 km/sec only.[8]

6. SUMMARY

In February 2004 the NACO FP was successfully commissioned and ESO will offer it from P74 on (October 2004) in visitor mode. During the commissioning the technical reliability was verified, and the calibration procedures could be developed and optimized. The described calibration procedures allow for a blind line matching accuracy better than 1 Å for the complete tuning range. During nighttime commissioning successful observations of the planetary nebula IC 418 were performed and we achieved excellent results. The phase shift correction for this extended object was done following our described standard procedure and the achieved images reveal brilliant details in comparison with earlier FP observations at other AO systems.[9] Even if we have demonstrated that a phase shift correction is feasible without too much effort, we pointed out that the FP can simply be used as tunable filter within a circular region with a radius smaller than 4″.

The scientific potential covers a wide range of astrophysical topics. In particular, we underlined the exciting application on 3D structure analysis for extended objects at 50 mas resolution.

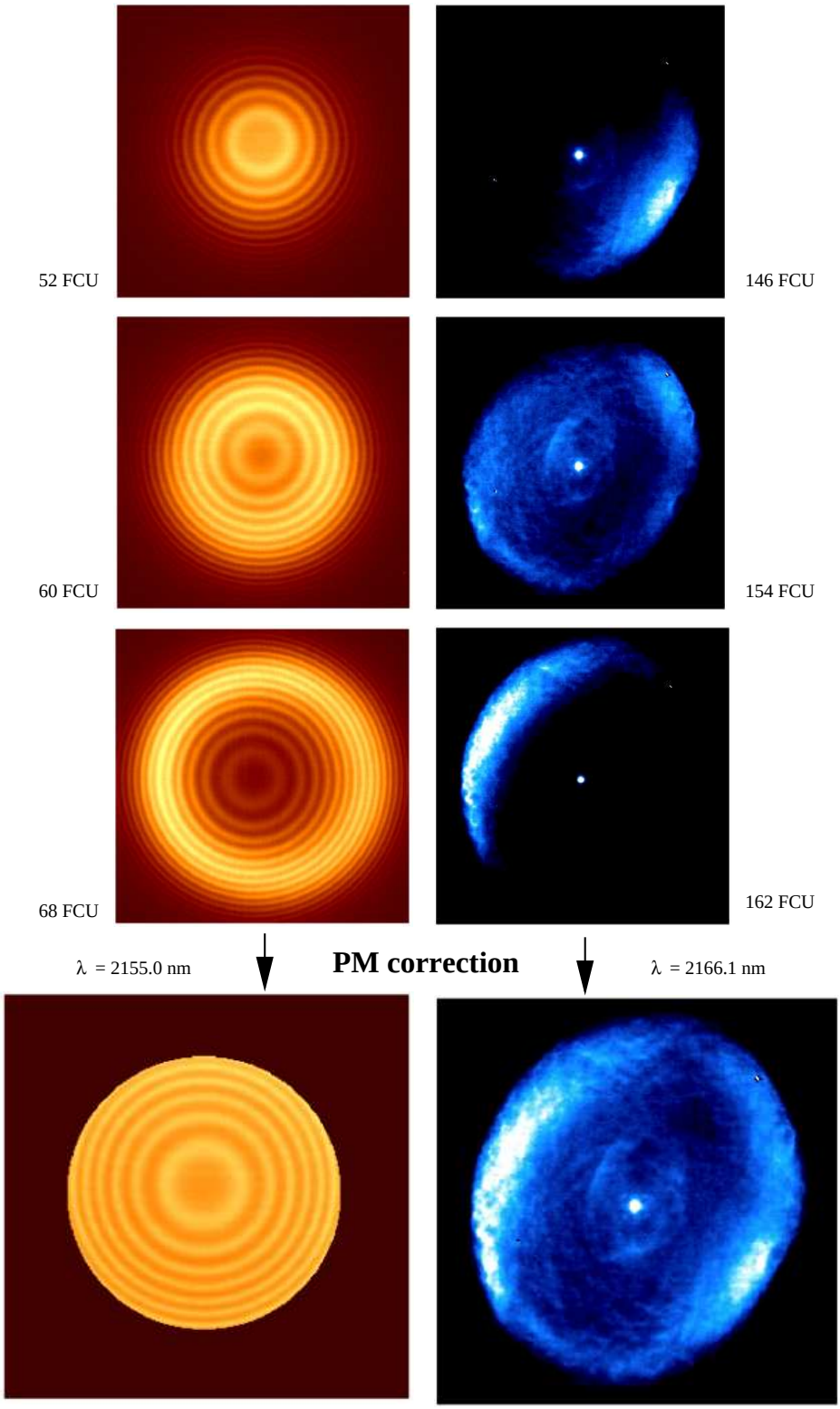

Figure 6. Scan of an Argon calibration line (comp. Fig. 2) and of the "spirograph" nebula IC 418 (diameter of major axis $14''$). For each sequence three frames out of the data cube are displayed. At the bottom the phase shift corrected frames at the line center of the calibration line (2154.0 nm) and the emission line (Brγ) are shown.

Table 5. NACO FP characteristics.

Manufacturer, Controller	Queensgate, CS100
Tuning range	2.00 - 2.50 μm
Order blocking filters	18 IB filters (60 nm FWHM) from 2.00 - 2.48 μm
Resolving power	1100
Bandpass	2.0 nm
Finesse	32
Reflectivity	91% (calculated with measured finesse and FP bandpass)
Δz for 1 nm	6-7 FCU (dependent of m, λ)
Tunable filter spot	Negligible phase shift for circular region with $r < 4''$.

ACKNOWLEDGMENTS

We wish to thank A. Kaufer (ESO) for his assistance during the commissioning time as well as T. Herbst (MPIA, Heidelberg) and P. Schuller (Harvard-Smithsonian Center for Astrophysics, Cambridge) for helpful remarks and discussions about this manuscript.

REFERENCES

1. R. Lenzen, M. Hartung, W. Brandner, G. Finger, N. N. Hubin, F. Lacombe, A. Lagrange, M. D. Lehnert, A. F. M. Moorwood, and D. Mouillet, "NAOS-CONICA first on sky results in a variety of observing modes," in *Instrument Design and Performance for Optical/Infrared Ground-based Telescopes*, A. Moorwood and M. Iye, eds., *Proc. SPIE* **4841**, pp. 944–952, Mar. 2003.
2. G. Rousset, F. Lacombe, P. Puget, N. N. Hubin, E. Gendron, T. Fusco, R. Arsenault, J. Charton, P. Feautrier, P. Gigan, P. Y. Kern, A. Lagrange, P. Madec, D. Mouillet, D. Rabaud, P. Rabou, E. Stadler, and G. Zins, "NAOS, the first AO system of the VLT: on-sky performance," in *Adaptive Optical System Technologies II*, P. Wizinowich and D. Bonaccini, eds., *Proc. SPIE* **4839**, pp. 140–149, Feb. 2003.
3. A. Lagrange, G. Chauvin, T. Fusco, E. Gendron, D. Rouan, M. Hartung, F. Lacombe, D. Mouillet, G. Rousset, P. Drossart, R. Lenzen, C. Moutou, W. Brandner, N. N. Hubin, Y. Clenet, A. Stolte, R. Schoedel, G. Zins, and J. Spyromilio, "First diffraction limited images at VLT with NAOS and CONICA," in *Instrument Design and Performance for Optical/Infrared Ground-based Telescopes*, M. Iye and A. Moorwood, eds., *Proc. SPIE*, pp. 860–868, Mar. 2003.
4. H. Jones, A. Renzini, P. Rosati, and W. Seifert, "Tunable Filters and Large Telescopes," *The Messenger* **103**, pp. 10–14, 2001.
5. M. Born and E. Wolf, *Principles of Optics*, Cambridge University Press, seventh ed., 1999.
6. S. Gordon, B. Koribalski, S. Houghton, and K. Jones, "A guide to TAURUS-2 Fabry-Perot data reduction," *Mon. Notices Royal Astron. Society* **315**, pp. 248–262, 2000.
7. A. V. Moiseev, "Reduction of CCD observation with scanning Fabry-Perot interferometer," *Bull. Spec. Astrophys. Obs.* **54**, 2002.
8. R. Williams, E. B. Jenkins, J. A. Baldwin, and B. Sharpee, "Comparative Absorption and Emission Abundance Analyses of Nebulae: Ion Emission Densities for IC 418," *Publ. Astron. Society Pacific* **115**, pp. 178–187, Feb. 2003.
9. B. Brandl, J. D. Smith, J. Wilson, J. Houck, and F. Eisenhauer, "Adaptive optics high spectral resolution imaging of the planetary nebula IC 418," in *Conference Paper, SPIE Proceedings, Vol. 3126, p. 561-568.*, pp. 561–568, Jan. 1997.